nature communications

Article

https://doi.org/10.1038/s41467-025-57097-x

Size-effect induced controllable Cu^0-Cu^+ sites for ampere-level nitrate electroreduction coupled with biomass upgrading

Received: 24 August 2024

Accepted: 8 February 2025

Published online: 10 March 2025

Check for updates

Yuxuan Lu[1,6], Feng Yue[2,6], Tianyang Liu[3,6], Yu-Cheng Huang[4], Feng Fu[2] ✉, Yu Jing[3] ✉, Hengquan Yang[1,5] ✉ & Chunming Yang[2] ✉

The synergistic Cu^0-Cu^+ sites is regarded as the active species towards NH_3 synthesis from the nitrate electrochemical reduction reaction (NO_3^-RR) process. However, the mechanistic understanding and the roles of Cu^0 and Cu^+ remain exclusive. The big obstacle is that it is challenging to effectively regulate the interfacial motifs of Cu^0-Cu^+ sites. In this paper, we describe the tunable construction of Cu^0-Cu^+ interfacial structure by modulating the size-effect of Cu_2O nanocube electrocatalysts to NO_3^-RR performance. We elucidate the formation mechanism of Cu^0-Cu^+ motifs by correlating the macroscopic particle size with the microscopic coordinated structure properties, and identify the synergistic effect of Cu^0-Cu^+ motifs on NO_3^-RR. Based on the rational design of Cu^0-Cu^+ interfacial electrocatalyst, we develop an efficient paired-electrolysis system to simultaneously achieve the efficient production of NH_3 and 2,5-furandicarboxylic acid at an industrially relevant current densities (2 A cm^{-2}), while maintaining high Faradaic efficiencies, high yield rates, and long-term operational stability in a 100 cm^2 electrolyzers, indicating promising practical applications.

Ammonia (NH_3), as a versatile industrial feedstock, is widely used for the production of nitrogen-based fertilizers, chemicals, pharmaceuticals, and polymers. Industrial NH_3 production relies on the Haber-Bosch process, under high temperature and high pressure (i.e. 350–450 °C and 150–200 bar)[1]. The carbon-intensive and highly energy-consuming Haber-Bosch process consumes about 1% of the world's annual energy output and generates 1.3% of global carbon dioxide emissions[2,3]. It is urgent and necessary to develop environmentally sustainable and affordable routes for NH_3 synthesis. Recently, the nitrate (NO_3^-) electrochemical reduction reaction (NO_3^-RR) has attracted increasing attention to produce NH_3 under mild conditions[4]. However, the performance of NO_3^-RR is hindered by the sluggish kinetics, which involves an eight-electron transfer, and the complex reaction pathways with multiple by-products, such as NO_2^-, N_2, N_2H_4, and H_2[5]. Moreover, the competitive hydrogen evolution reaction (HER) also hampers the Faradaic efficiency[6]. Thus, it is crucial to explore and develop a highly efficient electrocatalyst to compress the HER process and enable the desired conversion of NO_3^- into high-valued NH_3.

Recently, oxide-derived (OD) Cu catalyst has been widely studied due to excellent NO_3^-RR activity towards valuable NH_3[7]. Mechanistic studies have demonstrated that OD Cu catalyst would be electrochemically reduced to unsaturated Cu species under negative potential, and the synergistic Cu^0–Cu^+ sites is regarded as the active species

[1]Engineering Research Center of Ministry of Education for Fine Chemicals, School of Chemistry and Chemical Engineering, Shanxi Key Laboratory of the Green Catalytic Synthesis of Coal-based High Value Chemicals, Shanxi University, Taiyuan, PR China. [2]Shaanxi Key Laboratory of Chemical Reaction Engineering, College of Chemistry & Chemical Engineering, Yan'an University, Yan'an, Shaanxi, PR China. [3]Jiangsu Co-Innovation Centre of Efficient Processing and Utilization of Forest Resources, College of Chemical Engineering, Nanjing Forestry University, Nanjing, PR China. [4]National Synchrotron Radiation Research Center, Hsinchu, Taiwan. [5]Shanxi Research Institute of Huairou Laboratory, Taiyuan, PR China. [6]These authors contributed equally: Yuxuan Lu, Feng Yue, Tianyang Liu. ✉e-mail: fufeng@yau.edu.cn; yujing@njfu.edu.cn; hqyang@sxu.edu.cn; chunmingyang@yau.edu.cn

https://doi.org/10.1038/s41467-025-57097-x

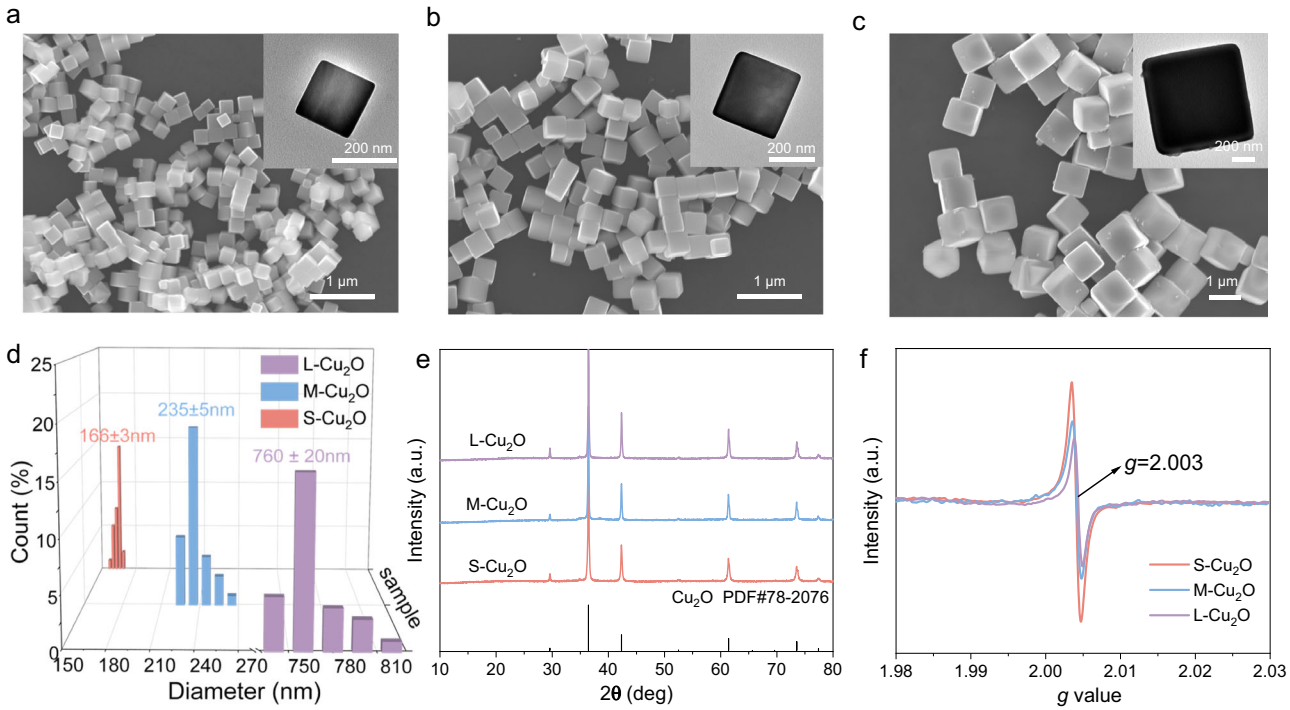

Fig. 1 | Structural characterizations of Cu_2O electrocatalyst. a–c SEM images of S-Cu_2O, M-Cu_2O, and L-Cu_2O. Inset is the corresponding TEM images. **d** Statistical size distribution of nanoparticles of S-Cu_2O, M-Cu_2O and L-Cu_2O. **e** XRD patterns of S-Cu_2O, M-Cu_2O, and L-Cu_2O. **f** EPR patterns of S-Cu_2O, M-Cu_2O and L-Cu_2O. Source data for **d**–**f** are provided as a Source Data file.

towards NH_3 synthesis during the NO_3^-RR process[8,9]. Therefore, numerous researches has been conducted to synthesize OD Cu catalyst with Cu^0–Cu^+ sites, and revealed the synergistic mechanism in the NO_3^-RR process[9–12]. The studies also showed that the interfacial motifs would determine the adsorption mode of nitro-intermediates and protons to significantly influence nitrogen selectivity[10,11]. However, the reaction mechanism and individual roles of interfacial Cu^0–Cu^+ sites are still unclear. One of the big obstacles is that it is challenging to effectively regulate the interfacial Cu^0–Cu^+ structure, since the structural motif of OD Cu is unstable under negative potential. Some studies have be devoted to control interfacial structure of Cu^0–Cu^+ sites by the strong metal-support interaction[13], while the electronic interaction between support and active Cu sites would bring to inevitable interference to identify the individual roles of interfacial Cu^0–Cu^+ sites. Therefore, with the goal of enhancing the NO_3^-RR performance of Cu-based electrocatalysts, it is of great necessary to understand the interface behavior and reaction mechanism by controllable Cu^+–Cu^0 sites.

Herein, we developed a feasible and efficient strategy to construct tunable Cu^+–Cu^0 interfacial motifs by modulating the size effects of Cu_2O nanocube catalysts. We revealed the design principle of Cu^+–Cu^0 pairs by correlating the macroscopic particle size with the microscopic localized coordinated structure properties by in situ electrochemical Raman and X-ray absorption near edge structure (XANES) characterization. Based on the controllable construction of the Cu^+–Cu^0 interfacial structure, we elucidated the individual and synergic roles of Cu^+ and Cu^0 sites during the NO_3^-RR process by combining electrochemical measurement and DFT calculations. Then, we developed an efficient paired-electrolysis system to simultaneously achieve the efficient production of NH_3 and 2,5-furandicarboxylic acid (FDCA) by coupling the cathodic NO_3^-RR process and anodic HMF electrochemical oxidation reaction (HMFOR) process at an industrially relevant current density, while maintaining high Faradaic efficiencies (FE_{NH3} 75.6%, FE_{FDCA} 71.2%), yield rates of NH_3 (5.20 mmol h^{-1} cm^{-2}) and FDCA (0.47 mmol h^{-1} cm^{-2}), and long-term operational stability (20 h) in a 100 cm^2 anion exchange membrane (AEM) electrolyzers, indicating promising practical applications. The techno-economic analysis demonstrates the potential of this system.

Results

Structural characterization

The Cu_2O nanocubes with different particle sizes are synthesized through the liquid phase reduction method, by adjusting the localized pH environment of the synthetic solution[14], three kinds of Cu_2O catalysts with different particle sizes were obtained, denoted as small Cu_2O nanocube (S-Cu_2O), medium Cu_2O nanocube (M-Cu_2O) and large Cu_2O nanocube (L-Cu_2O), respectively (Supplementary Fig. 1). The Cu^+–Cu^0 sites is controllably constructed by the in situ electrochemical reduction of Cu_2O nanocube precursors. The morphology and particle size of the Cu_2O nanocube precursors were characterized by scanning electron microscopy (SEM) and transmission electron microscopy (TEM), both Cu_2O sample exhibit cube-like nanocrystals (Fig. 1a–c), and the average size are concentrated in ~166 nm (S-Cu_2O), ~235 nm (M-Cu_2O) and ~760 nm (L-Cu_2O), respectively (Fig. 1d). Energy dispersive spectroscopic (EDS) elemental mapping further revealed that Cu and O elements are evenly distributed in the Cu_2O nanocubes and the ratio of Cu to O elements is close to 2:1. (Supplementary Fig. 2-4). The crystal structure of the Cu_2O nanocube was confirmed by high-resolution transmission electron microscopy (HRTEM) and X-ray diffraction (XRD). The lattice distance of 0.242 nm was found in the HR-TEM images (Supplementary Figs. 2–4), indicating that the dominant lattice plane is not influenced by the particle size, and (111) lattice plane is dominated on both Cu_2O samples. The XRD patterns confirmed the Cu_2O cubic phase (JCPDS: 78-2076) on both samples without the impurity phase (Fig. 1e).

X-ray photoelectron spectroscopy (XPS) was used to investigate the chemical states and electronic structure of Cu and O on the various Cu_2O nanocubes (Supplementary Fig. 5). In Cu 2*p* XPS spectrum, there are two peaks in both Cu_2O samples at 952.42 and 932.6 eV, which are attributed to Cu^+/Cu^0 species (Supplementary Fig. 6)[15]. Further, the

Auger electron spectroscopy (AES) was employed to distinguish Cu^+ and Cu^0 (Supplementary Fig. 7), it was found that Cu^+ (~569.6 eV) characteristic Auger peaks dominated on the Cu_2O surface, the signal of Cu^0 was not detected on the AES spectrum[9]. The content of surface oxygen species was identified by the O 1*s* XPS spectra (Supplementary Fig. 8), it is interesting that the higher content of chemisorbed oxygen groups (~531.0 eV), which belonged to defect-oxide groups, was found on the M-Cu_2O and S-Cu_2O sample[16]. The concentration of defect sites was further evaluated by the electron paramagnetic resonance (EPR), a representative EPR signal of $g = 2.003$ was found in both Cu_2O samples (Fig. 1f), revealing the electron trapped by oxygen vacancies[9]. The sequence of signal intensity is S-Cu_2O > M-Cu_2O > L-Cu_2O, indicating the higher content of oxygen vacancies on the small-size Cu_2O nanocubes, which is consistent with the XPS results. According to the principle of surface chemistry, the nanosized material not only shows a higher specific surface area, but also exposes higher content of unsaturated coordination sites, such as grain boundaries and edge sites, on the surface, and the concentration of unsaturated coordination sites is negatively related to the crystal size of materials. Therefore, it is rational speculate that the negative correlation of the concentration of defect sites and the particles size of Cu_2O nanocubes.

Then, the Cu^0–Cu^+ sites was constructed by a constant potentiostatic reduction on Cu_2O precursor in 1 M KOH and 0.1 M NO_3^- solution (pH =13.8) under a negative potential of −0.6 V vs RHE, ensuring to acquire the stable Cu-Cu^+ interfacial sites. The morphology structure and composition was observed in the SEM and TEM images, it was found that the Cu_2O catalysts retained the morphology of the nanocube, while the surface roughness increased after the electrochemical reduction process (Supplementary Figs. 9–12). Then, the structural evolution is investigated by the XRD patterns and HRTEM images, the results show that the crystal structure of Cu_2O and Cu could be simultaneously observed on both Cu_2O samples, indicating that the Cu_2O precursor is partially transferred to metallic Cu species for the formation of Cu/Cu_2O interface structure during the electrochemical reduction process (Supplementary Figs. 10–13), the as-obtained Cu_2O catalysts with Cu/Cu_2O interface structure is denoted as S-Cu/Cu_2O, M-Cu/Cu_2O, and L-Cu/Cu_2O, respectively.

Further, the in situ Raman spectroscopy was conducted to identify the dynamic phase transformation during the electrochemical reduction process. As shown in Fig. 2a and Supplementary Fig. 14, the characteristic peaks at 147, 218, 415, and 639 cm^{-1} were observed at the open circuit potential, which is attributed to the T_{1u}, E_u, A_u, and T_{2g} structural mode of Cu_2O precursors[17]. When the bias potential is tuned to −0.6 V_{RHE}, the signal of Cu_2O is rapidly dropped in the first two minutes and gradually tends to be stable, suggesting the structural evolution of Cu_2O to Cu/Cu_2O interface structure. The relative intensity of the Cu_2O signal could be used for evaluating the relative content of Cu_2O and identifying the Cu/Cu_2O interfacial structure after the electrochemical reduction process. Interestingly, the relative intensity follows the order of S-Cu/Cu_2O < M-Cu/Cu_2O < L-Cu/Cu_2O (Fig. 2b), indicating that the small particle size Cu_2O (S-Cu_2O), which owns a high concentration of defect sites, is more tended to transform to metallic Cu under electroreduction process.

Though in situ Raman spectroscopy is an efficient strategy to identify the bending mode for Cu–O bonds, it is difficult to accurately identify metallic Cu species during the electrochemical reduction process. Thus, the electronic structure and valence states of the Cu/Cu_2O structure is carefully evaluated by the AES spectrum. By quantifying the content of Cu^+ and Cu^0 in the Cu LMM spectra (Fig. 2c), the highest proportion of Cu^0 was found in S-Cu/Cu_2O is 78.9%, followed by M-Cu/Cu_2O (53.1%) and L-Cu/Cu_2O (38.4%), which is consistent with the in situ Raman spectra. Further, the XANES and extended X-ray absorption fine structure (EXAFS) were used for investigating the coordination environment and local electronic structure of Cu_2O catalysts after electroreduction (Fig. 2d, e). The secondary adsorption band (8983 eV), corresponding to a $1s \rightarrow 4p$ transition concurrent with ligand to metal charge transfer character, is used to evaluate the coordination structure of Cu^0–Cu^+ sites in XANES spectra[18]. After the electrochemical reduction process, the lower intensity of the secondary adsorption band was found on both Cu_2O samples, suggesting the appearance of unsaturated coordination structures. It was found that the S-Cu/Cu_2O shows the lowest adsorption intensity than M-Cu/Cu_2O and L-Cu/Cu_2O indicates a high degree of local structural disorder with a low oxidation state. Further, the fine coordination environment and geometric interface structure on the Cu^0–Cu^+ sites is observed in the EXAFS spectra. As shown in Fig. 2e, the characteristic coordination shell of the Cu–O bond (~1.5 Å) and Cu–O–Cu bond (~2.8 Å) were observed in Cu_2O precursors[19]. Interestingly, after reduction electrolysis, an extra coordination shell was found at ~2.5 Å[20], which contributed to the Cu^0–Cu bond on the metallic Cu species, indicating the appearance of Cu^0–Cu^+ interfacial structure during the electroreduction process. To accurately identify the fine coordination structure, the EXAFS spectra were fitted according to the optimal structure parameters, the corresponding fitting curves and structural information are displayed in Supplementary Figs. 15 and 16 and Supplementary Table 1. According to the EPR results, the S-Cu/Cu_2O has the higher concentration of unsaturated coordination structure, confirmed by the coordination number in Fig. 2f. The unsaturated defect Cu–O species on the Cu_2O surface, which own higher surface energy, tended to be reduced to metallic Cu species during the electrochemical reduction process. Thus, it was found that the coordination number (CN) of the Cu–O–Cu bond is dramatically reduced to metallic Cu species on S-Cu/Cu_2O with the appearance of the higher content of the Cu–Cu bond (Fig. 2f), indicating that the formation of metallic-Cu-dominated Cu/Cu_2O interface structure after the electroreduction process. On the contrary, owing to low defect concentration on large-sized Cu_2O, we found that the Cu_2O is slightly reduced to metallic Cu species on L-Cu/Cu_2O sample to form Cu^+-dominated Cu/Cu_2O interface structure. Therefore, by rational tuning the particle size of Cu_2O precursors, the Cu/Cu_2O interface structure with a flexible ratio of Cu^0 and Cu^+ could be effectively constructed.

Electrocatalytic performance for ammonia synthesis

Above, the electrocatalyst with Cu/Cu_2O interface structure has been constructed by modulating the size effect of Cu_2O catalysts. Then, the NO_3^-RR performance of as-synthesized Cu/Cu_2O catalysts was studied in a standard three-electrode H-type electrolytic cell. The electrochemical behavior was identified by the linear sweep voltammetry (LSV) curve. In the 1 M KOH solution, L-Cu/Cu_2O exhibits higher hydrogen evolution reaction (HER) activity than M-Cu/Cu_2O and S-Cu/Cu_2O (Supplementary Fig. 17), which is attributed to the higher content of Cu^+ species on the L-Cu/Cu_2O. The Cu^+ species has a lower energy barrier for the water-dissociation process than the Cu^0 species, resulting in rapid HER dynamics[21]. The NO_3^-RR performance is evaluated in the 1 M KOH with 0.1 M KNO_3 solution. As shown in Fig. 3a, the M-Cu/Cu_2O exhibits a higher current density than S-Cu/Cu_2O and L-Cu/Cu_2O, which is inconsistent with HER activity, indicating that the NO_3^-RR activity is not only influenced by the formation of adsorbed *H from water dissociation, but also strongly related to the adsorption of NO_3^- and NO_3^-RR intermediates. The intrinsic NO_3^-RR performance was evaluated by normalized by the electrochemically active surface area (ECSA), which investigated by non-faradaic double layer capacitance (C_{dl}) in Supplementary Fig. 18. It was found that M-Cu/Cu_2O still shows the best intrinsic activity, indicating that the M-Cu/Cu_2O has the optimal Cu^0–Cu^+ interface structure for catalyzing NO_3^-RR process (Supplementary Fig. 19). To investigate the NO_3^-RR dynamic process, the Tafel slope and electrochemical impedance spectroscopy (EIS) were conducted. The results of Tafel slopes shown that the M-Cu/Cu_2O has a faster electron transfer rate and rapid kinetics for NO_3^-RR

https://doi.org/10.1038/s41467-025-57097-x

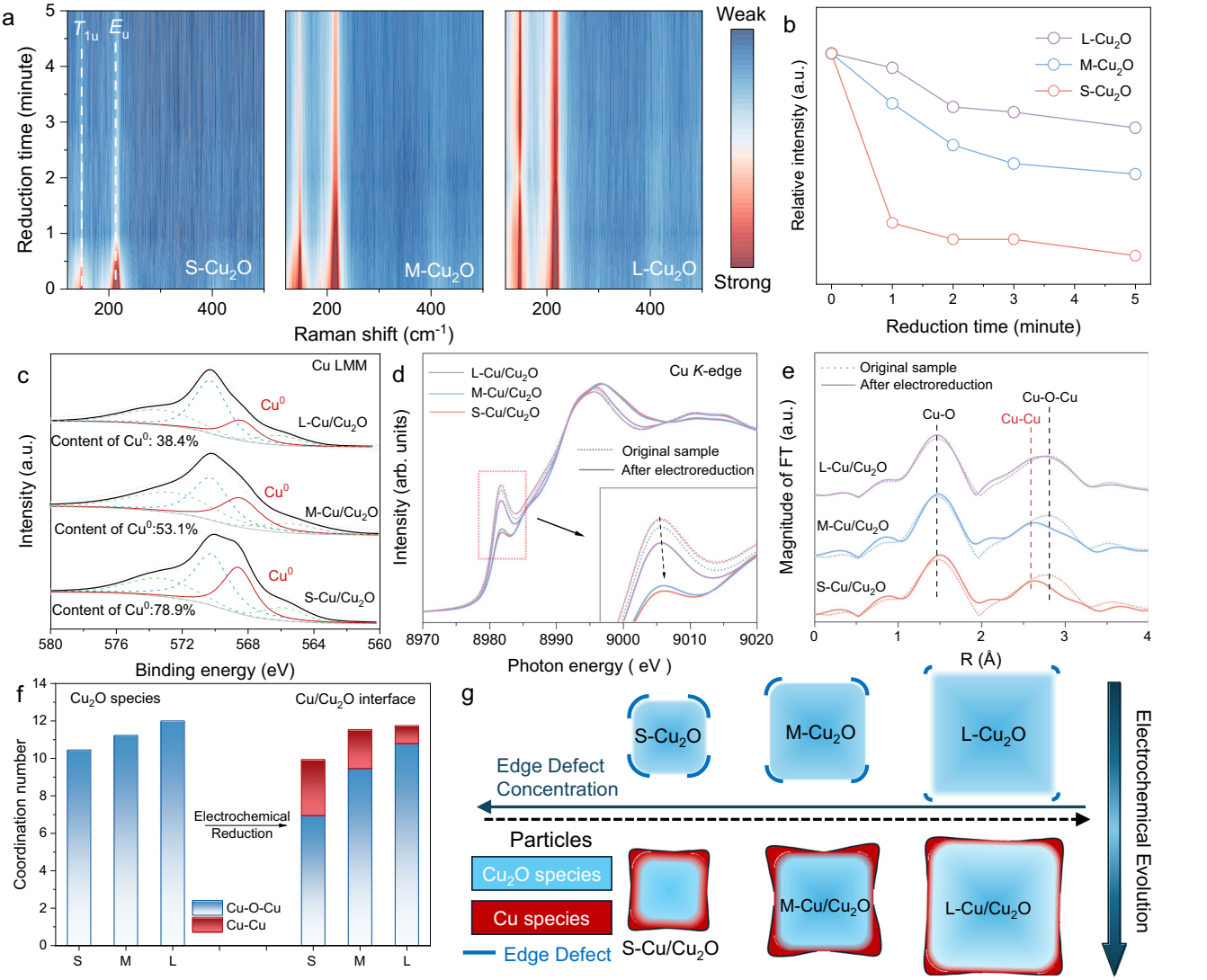

Fig. 2 | The identification of dynamic reconstruction of Cu_2O nanocubes. a In situ Raman spectra collected during the electrochemical reduction process on various Cu_2O samples. **b** The relationship between the intensity of characterized Raman signals and the time of electrochemical reduction. **c** AES spectra of Cu LMM over various Cu_2O nanocube catalysts after the electrochemical reduction process. **d** Normalized Cu K-edge XANES spectra. Inset is the magnification of Cu K-edge spectra. **e** Fourier transforms of Cu K-edge EXAFS spectra with optimal fitting results for various Cu_2O nanocube catalysts after electrochemical reduction process. **f** Structural coherence changes in EXAFS coordination number of Cu–Cu bonds and Cu–O–Cu bonds. **g** Schematic diagram of structural transformation of Cu_2O with different sizes. Source data for **a**–**f** are provided as a Source Data file.

(Supplementary Fig. 20). The electrochemical impedance was performed and fitted by optimal equivalent circuit, and the resistance of each component was shown in Supplementary Table 2. M-Cu/Cu_2O showed the lowest charge transfer resistance (R_{ct}), indicating that the appropriate Cu^0–Cu^+ interface structure would accelerate the charge transfer process and promote the NO_3^-RR kinetics (Supplementary Fig. 21).

The performance for the transformation of NO_3^- to NH_3 is evaluated by the electrochemical chronoamperometry measurement over S-Cu/Cu_2O, M-Cu/Cu_2O, and L-Cu/Cu_2O. The substrates, intermediates, and products were quantified by ultraviolet-visible (UV–vis) spectrophotometry, and the calibration curves are displayed in Supplementary Figs. 22–24. It was found that M-Cu/Cu_2O exhibits a maximum NH_3 Faradaic efficiency (FEs) of 95% at −0.2 V_{RHE} in Fig. 3b, which is much higher than that of S-Cu/Cu_2O (80%) and L-Cu/Cu_2O (86%). Moreover, an increasing yield rate of NH_3 and NO_3^- reduction rate was observed with the increase of applied negative potentials (Fig. 3c and Supplementary Fig. 25), while reached 0.29 mmol h^{-1} mg^{-1} and 0.25 mmol h^{-1} mg^{-1} towards NO_3^- reduction and NH_3 production, respectively, at the potential of −0.2V_{RHE} on M-Cu/Cu_2O, which is better than recently reported NO_3RR electrocatalysts (Fig. 3d and Supplementary Table 3). To enhance the reliability of size strategy, the M2-Cu/Cu_2O is synthesized with size (~402 nm) between M-Cu/Cu_2O and L-Cu/Cu_2O (Supplementary Fig. 26). Then, the electrocatalytic NO_3^-RR performance towards NH_3 production is evaluated in the 1 M KOH with 0.1 M KNO_3 solution. As shown in Supplementary Fig. 27, the NH_3 Faradaic efficiency (FEs) of M2-Cu/Cu_2O (87.6%) is slightly lower than M-Cu/Cu_2O (95%) and higher then L-Cu/Cu_2O (86%), indicating that size-effect strategy is convincing.

To confirm the adaptability of NH_3 production capability, the NO_3RR performance was studied at different NO_3^- concentrations over M-Cu/Cu_2O catalysts (Fig. 3e). It was found that the FE of NH_3 would also keep ~80% in a low concentration of NO_3^- solution (5 mM), indicating that M-Cu/Cu_2O also has a potential application prospect in the electroreduction of wastewater to NH_3. Furthermore, it was found that the NH_3 FE and yield rate remained stable after 10 electrolytic cycles (Fig. 3f and Supplementary Fig. 28). Notably, we observed that the crystal structure and phase composition of M-Cu/Cu_2O catalysts after

https://doi.org/10.1038/s41467-025-57097-x

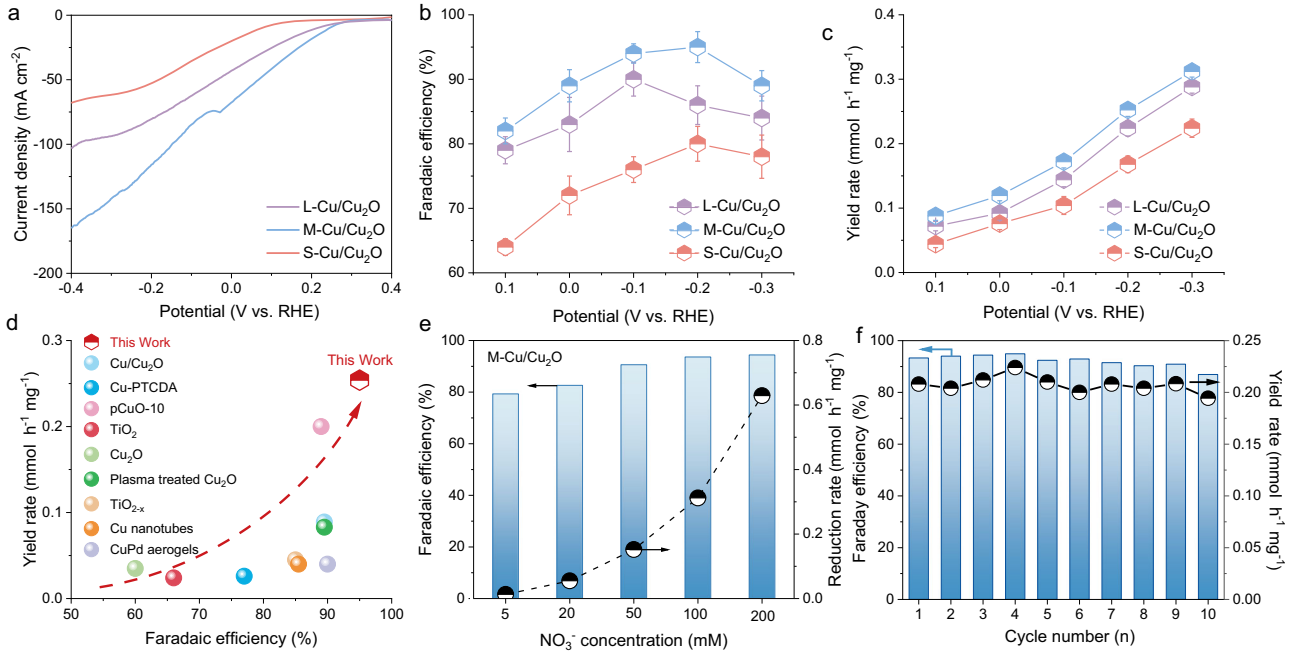

Fig. 3 | Electrocatalytic performance of NO_3RR over various Cu/Cu_2O catalysts. **a** LSV curves of various Cu/Cu_2O catalysts in the 1 M KOH with 0.1 M KNO_3 solution with the scan rate of 5 mV s^{-1}. The potential value is non-iR corrected. Faradaic efficiency (**b**) and yield rate (**c**) of NH_3 over various Cu/Cu_2O catalysts at different applied potentials. Data are presented as mean ± s.d. ($n = 3$) with the error bars representing the s.d. **d** Comparisons of NH_3 yield rates and Faraday efficiency between the M-Cu/Cu_2O and typically reported NH_3-synthesis electrocatalysts. **e** Faradaic efficiency of NH_3 production and NO_3^- reduction rates in the 1 M KOH with various concentrations of KNO_3 solution over M-Cu/Cu_2O catalysts at −0.2 V vs. RHE. **f** The Faradaic efficiency and yield rate of NH_3 over M-Cu/Cu_2O catalysts during the stability measurement. Source data for **a**–**f** are provided as a Source Data file.

electrolysis is similar to the fresh M-Cu/Cu_2O catalysts, indicating excellent stability of M-Cu/Cu_2O (Supplementary Fig. 29).

To verify the source of NH_3, controlled measurements were conducted by electrolysis in 1 M KOH solution with the absence of NO_3^-. It was found that the NH_3 produced is negligible, indicating that the acquirement of NH_3 originated from NO_3^-RR (Supplementary Figs. 30 and 31). Moreover, isotope labeling experiments were carried out with $K^{14}NO_3$ and $K^{15}NO_3$ as nitrates (Supplementary Fig. 32), and the products were determined by ^1H NMR spectroscopy. The results show that the typical two peaks of $^{14}NH_4^+$ and the typical three peaks of $^{15}NH_4^+$ in ^1H NMR, which confirms that the synthesized NH_3 comes from NO_3^- in solution rather than environmental contamination.

Mechanistic studies

Firstly, the possible reaction pathway and multiple intermediates were preliminarily evaluated via in situ Attenuated Total Refraction Fourier Transform Infrared Spectrometer (ATR-FTIR). As displayed in Fig. 4a and Supplementary Fig. 33, under the applied potential of −0.2 V_{RHE}, the peak at 1240 cm^{-1} and 1640 cm^{-1} were assigned to the N−O antisymmetric stretching of NO_2^- and the adsorption of *NO intermediates, and the doublets of 1423 cm^{-1} and 1457 cm^{-1} is attributed to NH_4^+ species[22,23], indicating that the pathway of $*NO_3^- \rightarrow *NO_2^- \rightarrow *NO \rightarrow *N \rightarrow *NH \rightarrow *NH_2 \rightarrow *NH_3$ is dominated on Cu/Cu_2O interfacial catalysts. Moreover, in situ differential electrochemical mass spectrometry (DEMS) is used to confirm the key intermediates during the NO_3RR process. As shown in Supplementary Fig. 34, the six possible NO_3RR intermediates could be observed on the DEMS signals at m/z 46 ($*NO_2$), 30 (*NO), 14 (*N), 15 (*NH), 16 ($*NH_2$), and 17 ($*NH_3$), respectively[24].

To identify the mechanism of NO_3^-RR on various Cu^0–Cu^+ interfacial catalysts, the product distribution of NO_3^-RR is evaluated at the applied potential of −0.2 V_{RHE}, it was found that the M-Cu/Cu_2O shows the highest NH_3 selectivity (93.6%) and NO_3^- conversion (86.2%) than S-Cu/Cu_2O and L-Cu/Cu_2O in Fig. 4b. Besides, the production of NO_2^-, derived from two-electron NO_3^- reduction process, is founded in the solution, which is attributed to the weakly reduction ability of NO_2- to NH_3. Further, by revealing potential-dependent production selectivity, it was found that S-Cu/Cu_2O tended to generate NO_2^- at low potential, resulting in higher NO_2^- FEs than M-Cu/Cu_2O and L-Cu/Cu_2O at the same potential (Supplementary Fig. 35), suggesting that the NO_2^- electrochemical reduction step is sluggish on the metallic-Cu-dominated Cu/Cu_2O interface structure, which leads to the abundant NO_2^- accumulation during the NO_3^-RR process. On the contrary, the rapid NO_2^- electrochemical hydrogenation is observed on the Cu^+-dominated Cu/Cu_2O interfacial catalysts, indicating that the Cu_2O is the active species for the $NO_2^- \rightarrow NH_3$ process.

It is known that two possible mechanisms of NO_3^- reduction reaction: direct electron transfer process and atomic H*-mediated indirect reduction process. For the atomic *H-mediated indirect reduction process, the water molecule would be firstly dissociated to *H and *OH on the surface of electrode, then a sequential electrochemical NO_3^- hydrogenation process is conducted by utilizing the adsorbed *H species. Different from the *H-mediated pathway, the NO_3^- adsorbed on catalysts would be electrochemically reduced by directly accepting electrons from catalysts without the involvement of water dissociation via the indirect reduction process. The electron spin resonance (ESR) is used to confirm the pathway during the NO_3^->RR process. Without adding NO_3^- in catholyte, the ESR spectra display typical 9 signals with intensity ratios of 1:1:2:1:2:1:2:1:1 (Fig. 4c), which confirms the formation of DMPO-H in the solution. However, when NO_3^- was added to the solution, the typical 9 signals were decreased (Fig. 4d), indicating that the adsorbed H* is consumed by the NO_3^-RR intermediates via atomic *H-mediated indirect reduction pathways over various Cu/Cu_2O catalysts. The sequence of DMPO-H signal intensity is S-Cu/Cu_2O < M-Cu/Cu_2O < L-Cu/Cu_2O, indicating Cu_2O species is tended to produce sufficient atomic *H adsorbed to participate in the hydrogenation of NO_3RR intermediates. The quenching experiments are conducted to identify the possible pathway on the various Cu-Cu_2O interfacial catalysts, and tertiary butyl alcohol (TBA)

https://doi.org/10.1038/s41467-025-57097-x

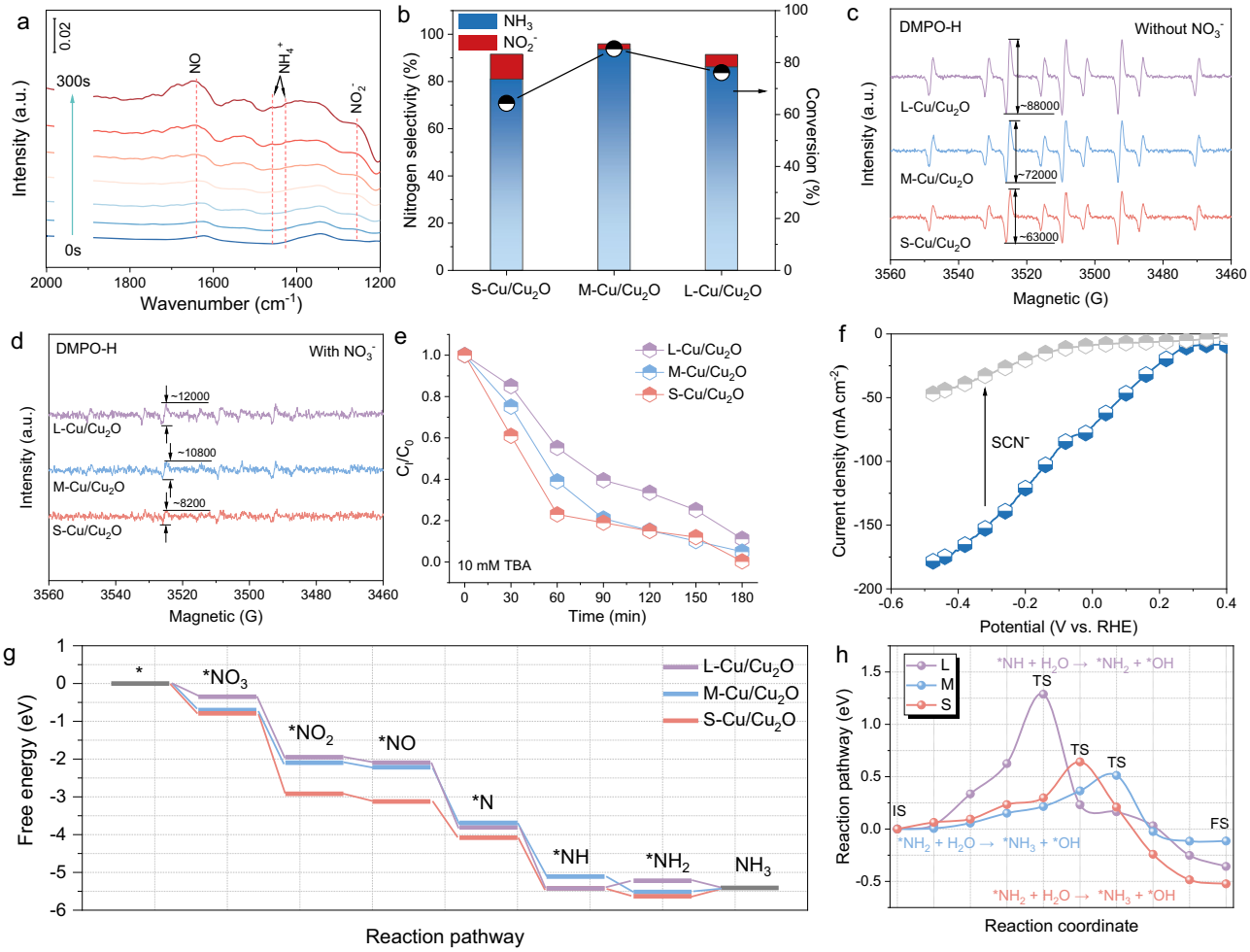

Fig. 4 | Mechanistic studies. a In situ FTIR spectra of M-Cu/Cu_2O catalyst during the nitrate reduction at various electrolytic times. **b** The evaluation of nitrogen selectivity and conversion rate over various Cu/Cu_2O catalysts at −0.2 V vs. RHE. **c**, **d** ESR spectra of DMPO adducts over various Cu/Cu_2O nanocube catalysts in the absence and presence of nitrate, the signal is collected after 15 min electrolysis at -0.2 V vs. RHE. **e** The transformation of NO_3^- over various Cu/Cu_2O nanocube catalysts with the presence of 10 mM TBA solution. **f** LSV curves of M-Cu/Cu_2O catalyst in the absence and presence of SCN^- solution. The potential value is non-iR corrected. **g** Gibbs free energy diagrams of the conversion of nitrate to ammonia over various Cu/Cu_2O catalysts; **h** the kinetic energy barriers of potential limiting steps over the various Cu/Cu_2O catalysts with CI-NEB method. Source data for **a**–**h** are provided as a Source Data file.

serves as a scavenger to capture atomic *H[25]. As shown in Fig. 4e, a decrease of NO_3^- kinetics on various Cu/Cu_2O catalysts was observed when 10 mM TBA was added into the solution, indicating that the atomic *H-mediated indirect reduction pathway is dominated. Compared to S-Cu/Cu_2O, M-Cu/Cu_2O and L-Cu/Cu_2O catalysts showed a rapid NO_3^- RR kinetics suggesting that Cu_2O species would provide sufficient atomic hydrogen for NO_3RR process, which is consistent with ESR results.

Besides, it is expected to identify the roles of Cu sites on the Cu^0–Cu^+ interfacial catalysts, a poisoning experiment was implemented using KSCN species[19]. Since the SCN^- is a strongly Lewis alkalinity, which would be selectively adsorbed on the metallic Cu sites and competed with NO_3^-, when SCN^- ions were added to the solution, the current density of NO_3RR decreased sharply (Fig. 4f), suggesting that the metallic Cu sites, in Cu^0–Cu^+ interface, play a vital role during the NO_3^-RR process.

Further, the DFT calculations were performed to elucidate the mechanism over the Cu^0–Cu^+ interface structure. Owing to strong electron correlation, the Hubbard-U parameter is used to prevent the delocalization of Cu *d*-orbitals. To accurately simulate the Cu^0–Cu^+ interface structure, the model of S-Cu/Cu_2O, M-Cu/Cu_2O, and L-Cu/Cu_2O catalysts is constructed and optimized based on the atomic ratio of Cu^0/Cu^+ species according to the AES and EXAFS results (detailed in the Supplementary information and Supplementary Data 1). Based on the ATR-FTIR results, the pathway of $*NO_3^- \rightarrow *NO_2^- \rightarrow *NO \rightarrow *N \rightarrow *NH \rightarrow *NH_2 \rightarrow *NH_3$ is proposed to investigate the reaction mechanism, and the optimal adsorption configuration of the reaction intermediates on various Cu/Cu_2O catalysts is displayed in Supplementary Figs. 36–40.

The adsorption behavior of NO_3^- reactant is investigated on the active Cu^0–Cu^+ sites, it was found that NO_3^- tends to adsorb on the metallic Cu^0 sites rather than Cu^+ sites or Cu^0–Cu^+ interface sites over various Cu/Cu_2O catalysts (Supplementary Fig. 36). Owing to the oxyphility of metallic Cu species, its tends to produce strong binding interactions with oxygenated species, resulting to the strong adsorption of NO_3^- reactant (Supplementary Fig. 37)[11,26]. It was found that the NO_3^- adsorption energy of L-Cu/Cu_2O (−0.35 eV) is lower than M-Cu/Cu_2O (−0.70 eV) and S-Cu/Cu_2O (−0.79 eV), suggesting that introduction of Cu_2O benefits to weaken the NO_3^- adsorption on the surface of Cu sites. The open circuit potential (OCP) measurement is also used to identify the adsorption of NO_3^- on the various Cu/Cu_2O electrocatalysts[27,28]. After the injection of KNO_3, the S-Cu/Cu_2O (0.14 V) showed a significant decrease in OCP than the M-Cu/Cu_2O (0.11 V) and L-Cu/Cu_2O (0.06 V), indicating that Cu^+ helps to weaken NO_3^-

https://doi.org/10.1038/s41467-025-57097-x

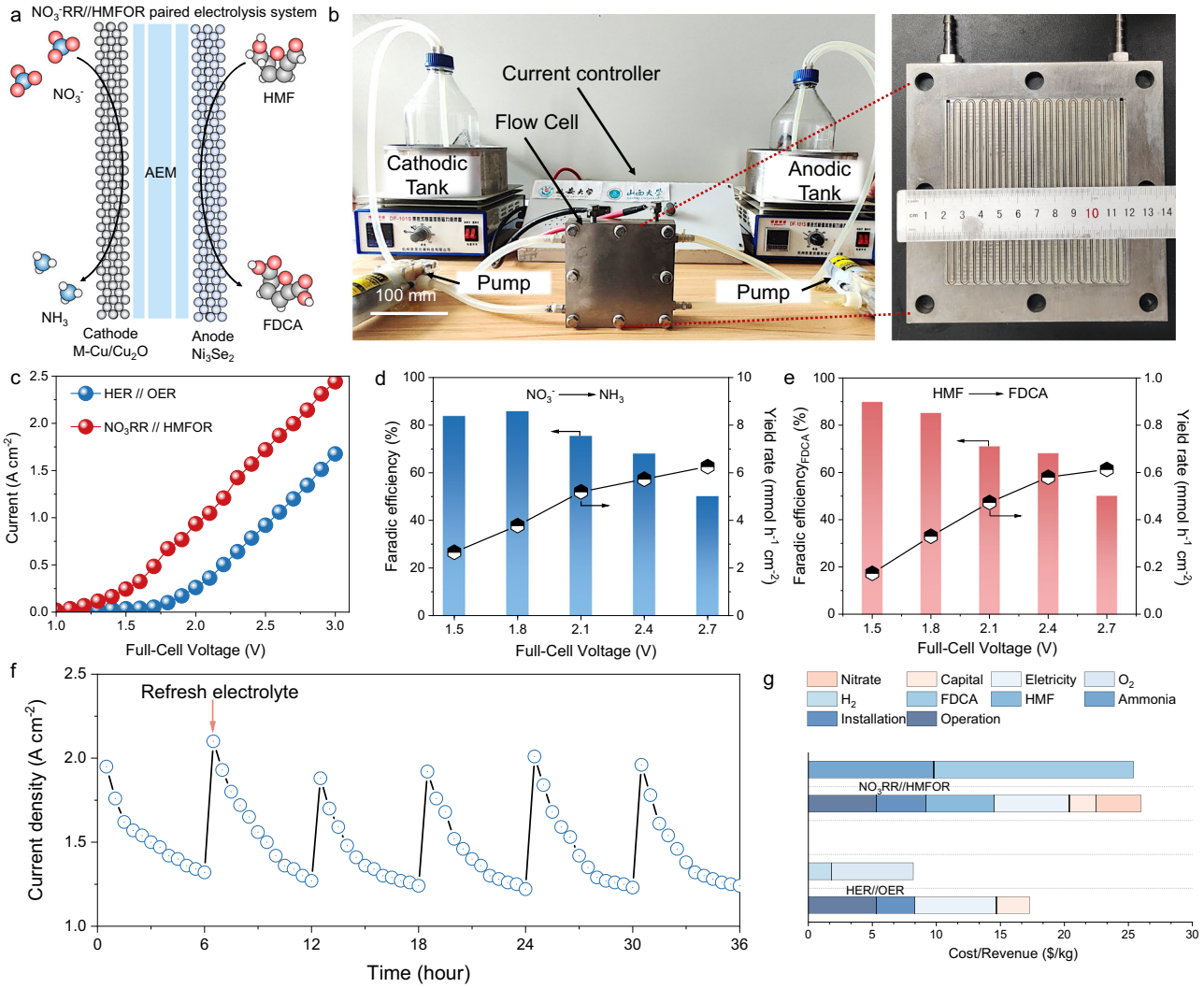

Fig. 5 | Paired-electrolysis system and techno-economic analysis. a, **b** Scheme and digital photo of NO_3^-RR//HMFOR paired-electrolysis system. **c** The LSV curves of overall water splitting systems and NO_3^-RR//HMFOR Paired-electrolysis system. Potential-dependent Faradaic efficiency and yield rate of NH_3 (**d**) and FDCA (**e**) in AEM electrolyzer. **f** Stability measurement of NO_3^-RR//HMFOR Paired-electrolysis system at the current density of 2 A cm^{-2}. **g** Techno-economic analysis of NO_3^-RR//HMFOR paired-electrolysis system. Source data for **c**–**g** are provided as a Source Data file.

adsorption (Supplementary Fig. 41), which is consistent with the results of DFT calculation.

Then, according to the proposed reaction pathway, the free energy of NO_3RR was investigated to identify the mechanism of synergistic Cu^0–Cu^+ motifs on various Cu/Cu_2O electrocatalysts. As shown in Fig. 4g, it was found that the hydrogenation step of $*NH_2 \rightarrow *NH_3$ is regarded as the potential limiting step (PLS) on the M-Cu/Cu_2O and S-Cu/Cu_2O, while the hydrogenation step of $*NH \rightarrow *NH_2$ is considered as PLS on the L-Cu/Cu_2O. It is interesting that the free energy change of PLS for M-Cu/Cu_2O (0.11 eV) is slightly lower than S-Cu/Cu_2O (0.22 eV) and L-Cu/Cu_2O (0.20 eV), indicating that the NO_3RR process is thermodynamically favorable on the M-Cu/Cu_2O electrocatalysts. Moreover, owing to the high energy barrier (0.96 eV), we have excluded possible pathway of *NO coupling for the formation of nitrogen gas (N_2) on the M-Cu/Cu_2O materials (Supplementary Fig. 42).

It was noticed that the water-dissociation reaction ($H_2O \rightarrow *H + *OH$) process is crucial to provide atomic hydrogen species for the hydrogenation of NO_3RR intermediates[29,30], while the H_2O molecules may be competitive adsorbed on the surface of electrode. Therefore, we considered the adsorption and activation behavior of H_2O molecules, it was found that the dissociation of the H_2O molecule needs to overcome a high kinetic energy barrier of 1.21 eV on the M-Cu/Cu_2O (Supplementary Fig. 43). Such a high energy barrier clearly reflects the sluggish water-dissociation kinetics and poor HER activity (Supplementary Fig. 17). Besides, the OH^- species may also be competitive adsorbed on the Cu sites, we found that the direct reduction of adsorbed *OH species also requires endothermic 0.24 eV, which is higher than NO_3RR (0.11 eV), demonstrating that M-Cu/Cu_2O exhibits the high selectivity for NO_3RR.

Further, we also explore the kinetic energy barrier for the PLS of the different Cu/Cu_2O materials. As shown in Fig. 4h, the kinetic energy barrier of the PLS is 0.51 eV on the M-Cu/Cu_2O, which is lower than S-Cu/Cu_2O (0.64 eV), and L-Cu/Cu_2O (1.29 eV), indicating that the M-Cu/Cu_2O, with the optimal interface structure, is favorable in kinetics for NO_3 electrochemical reduction process.

Paired-electrolysis NO_3^-RR//HMFOR system

Traditional electrocatalytic nitrate reduction systems involve a cathodic nitrate reduction reaction and anodic oxygen production reaction (OER). Though the efficient transformation of NO_3^- to NH_3 has been achieved by modulating the size effect of the Cu_2O electrocatalyst, the sluggish anodic OER process would dramatically enhance the energy consumption for NH_3 production. Thus, it is expected to explore promising anodic reactions for the replacement of the OER

process to reduce energy consumption. The electrooxidation of 5-hydroxymethylfurfural (HMF) to 2,5-furandicarboxylic acid (FDCA) has been attracted to replace the traditional OER process to reduce cell voltage and achieve the production of high-value chemicals. Since the Ni-based catalyst has excellent performance of HMF electrochemical oxidation reaction (HMFOR), the Ni_3Se_4, as a representative Ni-based material[31,32], was selected as anode electrocatalyst to assemble a paired electrolysis NO_3^-RR//HMFOR system (Fig. 5a).

To further verify the NO_3^-RR coupled HMFOR strategy, a simple scale-up test was carried out in an AEM electrolytic cell with a working area of 100 cm^2, and the M-Cu/Cu_2O and Ni_3Se_4 served as cathode and anode catalyst, respectively. The crystal structure and morphology is characterized by XRD pattern, SEM, and TEM images in Supplementary Figs. 44 and 45, and the HMFOR performance is evaluated in Supplementary Fig. 46. Digital photos and structural diagrams of AEM are shown in Fig. 5b. When coupling anodic HMFOR process and cathodic NO_3RR process, the cell voltage is significantly reduced (Fig.5c), indicating that the high energy conversion efficiency of NO_3RR//HMFOR system. The product measurement was performed at the different applied potentials as shown in Fig. 5d, e. The highly NH_4^+ yield rates (5.20 mmol h^{-1} cm^{-2}) and FE (75.6 %) with excellent FDCA yield rates (0.47 mmol h^{-1} cm^{-2}) and FE (71.2 %) were achieved at the potential of 2.1 V. Moreover, the NH_4^+ and FDCA could be continuously and stably produced at the current density of 2 A cm^{-2}, indicating the excellent stability of this electrolysis system (Fig. 5f). Further, we assembled a product extraction system to extract the cathode product (NH_4^+) and the anode product FDCA from the electrolyte. The purified product was confirmed by the XRD pattern in Supplementary Fig. 47. Based on the above results, it can be determined that the NO_3RR//HMFOR system would significantly improve energy efficiency, ensuring the economy and practicability, TEA results show that the economic benefits generated by the system are greater than the cost input (Fig. 5g).

Discussion

In summary, we developed a promising strategy to achieve the controllable construction of Cu^0/Cu^+ interfacial structure by modulating the size effect of Cu_2O nanocube electrocatalysts. Combining the in situ electrochemical Raman and X-ray absorption near edge structure (XANES) characterization, the design principle of Cu^0–Cu^+ pairs has been revealed by correlating the macroscopic particle size with the microscopic localized coordinated structure properties. Based on the controllable construction of the Cu^0–Cu^+ interfacial structure, we elucidated the synergic roles of Cu^+ and Cu^0 sites during the NO_3^-RR process by combining electrochemical measurement and DFT calculations. The results reveal that Cu^0 is the main active site in the Cu^0–Cu^+ motifs, Cu^+ helps to weaken NO_3^- adsorption, provides atomic *H species to accelerate potential limiting step of the hydrogenation of NH_2 to NH_3. Based on the design of Cu^+–Cu^0 interfacial electrocatalyst, we developed an efficient NO_3^-RR//HMFOR paired electrolysis system to simultaneously achieve the efficient production of NH_3 and FDCA at an industrially relevant current density, while maintaining high Faradaic efficiencies (75.6% for NH_3, 71.2% for FDCA), yield rates (5.20 mmol h^{-1} cm^{-2} for NH_3, 0.47 mmol h^{-1} cm^{-2} for FDCA), and long-term operational stability (20 h) in AEM electrolyzers with an area of 100 cm^2. This work provides a strategy to design energy-effective and eco-friendly electrocatalysts for large-scale industrial electrolytic synthesis of high-value-added products.

Method

Chemical reagents

KNO_3 (Kermel, GR, 99%), KNO_2 (Kermel, GR, 99%) NH_4Cl (Aladdin, AR, 99%), 5-hydroxymethylfurfural (98%) were purchased from Energy Chemical. 5-hydroxymethyl-2-furancarboxylic acid (98%), 5-formyl-furancarboxylic acid (99%), 2,5-diformyfuran (98%), and 2,5-furandicarboxylic acid (98%) were obtained from Aladdin. $Cu(CH_3COO)_2{\cdot}H_2O$ (Aladdin, AR, 99%), L-Ascorbic acid (Macklin, AR, 99%), and NaOH (Macklin, AR, 99%) were used without further purification. Deionized water (UPR series super pure water purification system, resistivity >18.2 MΩ cm) was used to prepare all solutions.

Materials preparation

Synthesis of Cu_2O nanocubes. In a typical synthesis, a mixture of 10.0 mL of 0.009 M ascorbic acid solution and 16.0 mL of 0.113 M NaOH solution was added into 16.0 mL of 0.005 M copper acetate solution. The mixed solution was stirred vigorously for 30 min, enabling the solution became yellow and turbid, indicating the formation of Cu_2O nanocubes. Finally, the precipitates were collected and washed through centrifugation. All the experiments were carried out at room temperature (298 K).

Synthesis of Cu/Cu_2O nanocubes. The Cu/Cu_2O nanocubes were synthesized from Cu_2O nanocubes by a constant potentiostatic reduction process at the potential of −0.6 V vs RHE for 300 s in 1 M KOH and 0.1 M NO_3^- solution. This process was implemented in a three-electrode system, where carbon paper, loaded on the Cu_2O nanocubes, graphite rod, and Hg/HgO electrode was used as the working electrode, counter electrode, and reference electrode. After the electrochemical reduction process, the obtained Cu/Cu_2O nanocubes were washed with absolute ethanol and blown dry by nitrogen.

Materials characterization

XRD patterns were collected via an X-ray diffractometer (Shimadzu XRD-7000) using monochromatic Cu K_α radiation (λ = 1.5406 Å) to investigate the phase structure transformation. Scanning electron microscopy (SEM; JSM-7610F) and transmission electron microscopy (TEM; JEOL F200 equipped with energy dispersive spectrometer (EDS)) were employed to observe the microstructure and elemental distribution of the catalysts. The chemical composition and surface valence of the catalysts were analyzed through X-ray photoelectron spectroscopy with an Al-K_α X-ray source (E = 1486.6 eV, XPS, Thermo Scientific Escalab), and the binding energy was corrected with a C 1*s* spectral of 284.8 eV. Raman spectroscopy was collected on a laser Raman spectrometer (Horiba LabSpec6, 532 nm laser). The ultraviolet-visible (UV-Vis) absorbance spectra were measured on a spectrophotometer (Beijing Purkinje General T6 new century).

Electrochemical measurement

Typically, 1 mg catalyst was dispersed in a mixed solvent containing 500 μL of ethanol, deionized water (450 μL), and 50 μL of 5% Nafion solution. After ultrasonic treatment for 20 min, the catalyst slurry was dropped uniformly onto a piece of carbon paper (1 cm^2, 1 mg cm^{-2}). After drying at room temperature (298 K), the catalyst-covered carbon paper was utilized as the working electrode in NO_3^-RR measurements. The NO_3^-RR measurements were performed with a three-electrode system in an H-type electrochemical cell separated by Nafion 117 membrane using a CHI electrochemical workstation (CHI 760E) at room temperature (298 K). The Nafion 117 membrane was pre-treated by immersing it in water, 5% H_2O_2 solution, and 0.5 M H_2SO_4 at 80 °C for 1 h. The Cu/Cu_2O was used as the working electrode, a carbon rod as the counter electrode, and Hg/HgO as the reference electrode. The NO_3^-RR measurement was conducted in 1.0 M KOH with 0.1 M KNO_3 solution (pH was 13.8 ± 0.2, which determined by pH meter). All potentials were recorded against the reversible hydrogen electrode (RHE, $E_{RHE} = 0.0591 \times pH + 0.098\ V + E_{Hg/HgO}$) without special explanation. The linear sweep voltammetry (LSV) test was performed at a rate of 5 mV s^{-1}, and the potential was not iR corrected. Constant potential electrolysis was conducted at each potential for 3 h. Electrochemical surface area (ECSA) was calculated from scan rate dependence of CV with scan rates of 10–90 mV s^{-1}. The

electrochemical impedance spectroscopy (EIS) measurements were carried out with frequencies from 0.01 Hz to 100 kHz at an amplitude of 10 mV. For flow electrochemical measurement, the customized two-electrode flow cell (as shown in Fig. 5b) is used for the NO_3^-RR//HMFOR paired-electrolysis system, the cathode and anode were separated by a anion exchange membrane (Fumasep FAA-3-20), which is directly used for electrochemical measurement without pre-treatment, and the voltages was not iR corrected. The Ni_3Se_4, dropped on the carbon felt (10×10 cm^2, 2 mg cm^{-2}), and M-Cu_2O, dropped on the carbon felt (10×10 cm^2, 2 mg cm^{-2}), were used as anode and cathode, respectively. Catalyst inks (Ni_3Se_4 or M-Cu_2O, 200 mg) were prepared by dispersing catalyst powder in a mixture of isopropanol (10 mL), pure water (9 mL), and Nafion (1 mL). Subsequently, the catalyst inks were dropped on the carbon felt and dried at room temperature (298 K). The anodic electrolyte of 0.1 M HMF in 2.0 M KOH was prepared before pumping into the anode chamber with a flow rate of 20.0 mL min^{-1}, and the cathodic electrolyte of 0.1 M KNO_3 in 2.0 M KOH was prepared before pumping into the cathode chamber with a flow rate of 20.0 mL min^{-1}. The electrolyte pumping out from the anode and cathode were collected, and the product was analyzed using HPLC and UV–Vis, respectively.

Product quantification

The UV–Vis spectrophotometer was used to quantified the concentration of nitrate, nitrite, and ammonia by same colorimetric methods. In nitrate quantification, the electrolyte is neutralized and diluted to suitable concentrations. Then, 2 mL of 0.8 w% sulfamic acid solution, 2 mL of Nessler's reagent followed by 1 M HCl were added to the above solution. After standing at room temperature (298 K) for 20 min, record the absorbance at a wavelength of 420 nm with a UV–Vis spectrophotometer. In nitrite quantification, a mixture of p-aminobenzenesulfonamide (4 g), N-(1-Naphthyl) ethylenediamine dihydrochloride (0.2 g), ultrapure water (50 mL), and phosphoric acid (10 mL, 1.70 g mL^{-1}) was used as a color reagent. A certain amount of electrolyte was extracted from the cathodic chamber and diluted to suitable concentrations. Then, 0.1 mL of color reagent was added to the above solution to further react for 20 min. The absorbance was recorded at a wavelength of 540 nm. In ammonia quantification, Nessler's reagent was used as the color reagent to determine the quantification of ammonia. Firstly, a certain amount of electrolyte was extracted from the cathodic chamber and diluted to suitable concentrations. Then, 0.1 mL of potassium sodium tartrate solution ($\rho = 500$ g L^{-1}) and 0.1 mL Nessler's reagent were subsequently added into the above solution to further react for 20 min. The absorbance was recorded at a wavelength of 420 nm.

Calculation of the yield, selectivity, and Faradaic efficiency

The conversion of NO_3^- was calculated using:

$$\text{Conversion}(NO_3^-) = \Delta C_{NO_3^-} / C_0 \times 100\% \quad (1)$$

The selectivity of NH_3 and NO_2^- calculated using:

$$\text{Selectivity}(NH_3) = C_{NH_3} / \Delta C_{NO_3^-} \times 100\% \quad (2)$$

$$\text{Selectivity}(NO_2^-) = C_{NO_2^-} / \Delta C_{NO_3^-} \times 100\% \quad (3)$$

The yield of NH_3 was calculated using:

$$\text{Yield}(NH_3) = (C_{NH_3} \times V) / (M_{NH_3} \times t \times m) \quad (4)$$

The Faradaic efficiency was calculated using:

$$\text{Faradaic efficiency} = (8F \times C_{NH_3} \times V) / (M_{NH_3} \times Q) \times 100\% \quad (5)$$

Where C_{NH_3} and $C_{NO_2^-}$ are the concentration of NH_3 and NO_2^-, $\Delta C_{NO_3^-}$ is the concentration difference of NO_3^- before and after electrolysis, C_0 is the initial concentration of NO_3^-, V is the electrolyte volume, t is the electrolysis time, m is the mass of catalyst, F is the Faradaic constant (96,485 C mol^{-1}), Q is the total charge passing the electrode.

Theoretical simulation

All density functional theory (DFT) calculations were performed using the Vienna ab initio simulation package (VASP)[33]. The ion-electron interaction was described with the projector-augmented plane-wave (PAW) method[34]. The strongly correlated electronic states of Cu-3*d* orbitals were corrected via a DFT + U method. The effective Hubbard-*U* parameter (U_{eff}) for the Cu atom was set to be 5.0 eV[35]. The kinetic energy cutoff for the plane-wave expansion was set to 400 eV, and the Brillouin zone was sampled with $3 \times 3 \times 1$ for geometry optimization. All the structural models were fully relaxed to the ground state with the convergence of energy and forces setting to 5×10^{-5} eV and 0.05 eV Å^{-1}, respectively. DFT-D3 (D stands for dispersion) with the empirical correction in Grimme's scheme was employed to describe van der Waals (vdW) interactions[36]. Solvation effect was considered with the Poisson-Boltzmann implicit solvation model, and the dielectric constant of water was set to 80[37].

The Cu_2O and Cu crystallographic information files were downloaded from the Materials Project crystal material library. For the Cu_2O catalyst, the typical (111) slab with a $(3 \times 3 \times 3)$ supercell was constructed; the top two layers and NO_3RR intermediates were fully relaxed, while the bottom layer was fixed. The bulk Cu was established as nanoclusters to represent the metal Cu species formed during the NO_3RR progress. Especially, considering the different structure the Cu^0–Cu^+ sites, we combine the Cu_2O (111) planes and Cu clusters to build the three types of Cu/Cu_2O catalysts. Using the Cu cluster of 15, 27, and 43 atoms, to represent L-Cu/Cu_2O, M-Cu/Cu_2O, and S-Cu/Cu_2O according to according to the Auger electron spectroscopy results. The length of the vacuum layer in the Z direction was set to 15 Å to avoid the interactions between periodic images. The Gibbs free energy of each species was calculated by the computational hydrogen electrode (CHE) model[38]. Here, the chemical reaction considered can be summarized with the reaction equations below.

$$* + NO_3^- \rightarrow {}^*NO_3 + e^- \quad (6)$$

$$*NO_3 + H_2O(l) + e^- \rightarrow *NO_2 + 2OH^- \quad (7)$$

$$*NO_2 + H_2O(l) + 2e^- \rightarrow *NO + 2OH^- \quad (8)$$

$$*NO + H_2O(l) + 2e^- \rightarrow *N + 2OH^- \quad (9)$$

$$*N + H_2O(l) + e^- \rightarrow *NH + OH^- \quad (10)$$

$$*NH + H_2O(l) + e^- \rightarrow *NH_2 + OH^- \quad (11)$$

$$*NH_2 + H_2O(l) + e^- \rightarrow *NH_3 + OH^- \quad (12)$$

$$*NH_3 \rightarrow NH_3(g) + * \quad (13)$$

Where * represents the active site. Then, the reaction free energy can be obtained with the equation below:

$$\Delta G = \Delta E + \Delta E_{ZPE} - T\Delta S \quad (14)$$

Where ΔE is the total energy difference before and after intermediate adsorbed, ΔE_{ZPE} and ΔS are the differences of ZPE zero-point energy and entropy, respectively, which can be obtained from the vibrational frequency calculations. T is room temperature (298 K). Besides, the climbing-image nudged elastic band (CI-NEB) method was used to simulate the energy barrier of the NO_3RR process[39].

Data availability

The data that support the findings of this study are available in the paper and its Supplementary Information. Source data for Figs. 1–5 are provided as a Source Data file. Source data are provided in this paper. Source data are provided with this paper.

References

1. Chen, J. G. et al. Beyond fossil fuel–driven nitrogen transformations. *Science* **360**, 6611 (2018).
2. Humphreys, J., Lan, R. & Tao, S. Development and recent progress on ammonia synthesis catalysts for Haber–Bosch process. *Adv. Energ. Sustain. Res.* **2**, 2000043 (2021).
3. Li, K. et al. Enhancement of lithium-mediated ammonia synthesis by addition of oxygen. *Science* **374**, 1593–1597 (2021).
4. Fu, X. et al. Continuous-flow electrosynthesis of ammonia by nitrogen reduction and hydrogen oxidation. *Science* **379**, 707–712 (2023).
5. Wang, D., Lu, X. F., Luan, D. & Lou, X. W. Selective electrocatalytic conversion of nitric oxide to high value-added chemicals. *Adv. Mater.* **36**, 2312645 (2024).
6. Long, J. et al. Direct electrochemical ammonia synthesis from nitric oxide. *Angew. Chem. Int. Ed.* **59**, 9711–9718 (2020).
7. Ren, Z., Shi, K. & Feng, X. Elucidating the intrinsic activity and selectivity of Cu for nitrate electroreduction. *ACS Energ. Lett.* **8**, 3658–3665 (2023).
8. Shen, Z. et al. Cu/Cu^+ synergetic effect in Cu_2O/Cu/CF electrocatalysts for efficient nitrate reduction to ammonia. *ACS Sustain. Chem. Eng.* **11**, 9433–9441 (2023).
9. Shi, Y. et al. In-situ reconstructed Cu/Cu_2O heterogeneous nanorods with oxygen vacancies for enhanced electrocatalytic nitrate reduction to ammonia. *Chem. Eng. J.* **479**, 147574 (2024).
10. Costa, G. F. et al. Identifying the active site of Cu/Cu_2O for electrocatalytic nitrate reduction reaction to ammonia. *Chem Catal* **4**, 100850 (2024).
11. Zhou, J. et al. Achieving efficient and stable electrochemical nitrate removal by in-situ reconstruction of Cu_2O/Cu electroactive nanocatalysts on Cu foam. *Appl. Catal. B Environ.* **317**, 121811 (2022).
12. Bai, L. et al. Electrocatalytic nitrate and nitrite reduction toward ammonia using Cu_2O nanocubes: active species and reaction mechanisms. *J. Am. Chem. Soc.* **146**, 9665–9678 (2024).
13. Yuan, X. et al. Controllable Cu^0-Cu^+ sites for electrocatalytic reduction of carbon dioxide. *Angew. Chem. Int. Ed.* **60**, 15344–15347 (2021).
14. Cao, Y., Xu, Y., Hao, H. & Zhang, G. Room temperature additive-free synthesis of uniform Cu_2O nanocubes with tunable size from 20 nm to 500 nm and photocatalytic property. *Mater. Lett.* **114**, 88–91 (2014).
15. Zhong, W. et al. Modulating surface oxygen species via facet engineering for efficient conversion of nitrate to ammonia. *J. Energy Chem.* **78**, 211–221 (2023).
16. Lu, Y. et al. Tailoring competitive adsorption sites by oxygen-vacancy on cobalt oxides to enhance the electrooxidation of biomass. *Adv. Mater.* **34**, 2107185 (2021).
17. Sander, T. et al. Correlation of intrinsic point defects and the Raman modes of cuprous oxide. *Phy. Rev. B* **90**, 045203 (2014).
18. Liu, X. et al. Self-supported copper oxide electrocatalyst for water oxidation at low overpotential and confirmation of its robustness by Cu K-edge X-ray absorption spectroscopy. *J. Phys. Chem. C* **120**, 831–840 (2016).
19. Pan, Y. et al. Unveiling the synergistic effect of multi-valence Cu species to promote formaldehyde oxidation for anodic hydrogen production. *Chem* **9**, 963–977 (2023).
20. Fan, Y. et al. Electrochemical synthesis of formamide by C–N coupling with amine and CO_2 with a high faradaic efficiency of 37.5%. *Chem* **10**, 2437–2449 (2024).
21. Qu, Y. et al. Heterostructured Co-doped-Cu_2O/Cu synergistically promotes water dissociation for improved electrochemical nitrate reduction to ammonia. *Small* **20**, 2308246 (2024).
22. Li, M. et al. Electrosynthesis of amino acids from NO and α-keto acids using two decoupled flow reactors. *Nat. Catal.* **6**, 906–915 (2023).
23. Butcher, Jr. D. P. & Gewirth, A. A. Nitrate reduction pathways on Cu single crystal surfaces: Effect of oxide and Cl^-. *Nano Energy* **29**, 457–465 (2016).
24. Han, S. et al. Ultralow overpotential nitrate reduction to ammonia via a three-step relay mechanism. *Nat. Catal.* **6**, 402–414 (2023).
25. Duan, W. et al. In situ reconstruction of metal oxide cathodes for ammonium generation from high-strength nitrate wastewater: Elucidating the role of the substrate in the performance of Co_3O_{4-x}. *Environ. Sci. Technol.* **57**, 3893–3904 (2023).
26. Wang, J. et al. Electrocatalytic nitrate/nitrite reduction to ammonia synthesis using metal nanocatalysts and bio-inspired metalloenzymes. *Nano Energy* **86**, 106088 (2021).
27. Pan, Y. et al. Electrocatalytic coupling of nitrate and formaldehyde for hexamethylenetetramine synthesis via C–N bond construction and ring formation. *J. Am. Chem. Soc.* **146**, 19572–19579 (2024).
28. Lu, Y. et al. Tuning the selective adsorption site of biomass on Co_3O_4 by Ir single atoms for electrosynthesis. *Adv. Mater.* **33**, e2007056 (2021).
29. Deng, X., Yang, Y., Wang, L., Fu, X. Z. & Luo, J. L. Metallic Co nanoarray catalyzes selective NH3 production from electrochemical nitrate reduction at current densities exceeding 2 A cm^{-2}. *Adv. Sci.* **8**, 2004523 (2021).
30. Wang, Y. et al. Enhanced nitrate-to-ammonia activity on copper–nickel alloys via tuning of intermediate adsorption. *J. Am. Chem. Soc.* **142**, 5702–5708 (2020).
31. Fangying, D., Menglei, Y. & Jian, Z. Paired electrolysis for inorganic small molecules reduction coupled with alternative oxidation reactions. *Chinese J. Org. Chem.* **44**, 809 (2024).
32. Wang, R. et al. Three-dimensional Ni_3Se_4 flowers integrated with ultrathin carbon layer with strong electronic interactions for boosting oxygen reduction/evolution reactions. *Chem. Eng. J.* **430**, 132720 (2022).
33. Kresse, G. & Hafner, J. Ab initio molecular dynamics for liquid metals. *Phys Rev B Condens Matter* **47**, 558–561 (1993).
34. Blochl, P. E. Projector augmented-wave method. *Phys. Rev. B Condens. Matter* **50**, 17953–17979 (1994).
35. Chang, C.-C., Ku, M.-S., Lien, W.-H. & Hung, S.-F. Unveiling the bonding nature of C3 intermediates in the CO_2 reduction reaction through the oxygen-deficient Cu_2O (110) surface— A DFT study. *J. Phys. Chem. C* **126**, 5502–5512 (2022).
36. Grimme, S. Semiempirical GGA-type density functional constructed with a long-range dispersion correction. *J. Comput. Chem.* **27**, 1787–1799 (2006).

37. Mathew, K., Sundararaman, R., Letchworth-Weaver, K., Arias, T. & Hennig, R. G. Implicit solvation model for density-functional study of nanocrystal surfaces and reaction pathways. *J. Chem. Phys.* **140**, 084106 (2014).
38. Nørskov, J. K. et al. Origin of the overpotential for oxygen reduction at a fuel-cell cathode. *J. Phys. Chem. B* **108**, 17886–17892 (2004).
39. Henkelman, G., Uberuaga, B. P. & Jónsson, H. A climbing image nudged elastic band method for finding saddle points and minimum energy paths. *J. Chem. Phys.* **113**, 9901–9904 (2000).

Acknowledgements

This work was supported by National Natural Science Foundation of China (Grant Nos. 22162025; 21925203; 22332002; 22402110; 22222304; 22403048), the Youth Innovation Team of Shaanxi Universities, the Program for Young Scholar Talents of Wenying in Shanxi University, the Program of Technology Innovation of Shanxi Province (2024L007), the Open and Innovation Fund of Hubei Three Gorges Laboratory (SK232001), the Regional Innovation Capability Leading Program of Shaanxi (2022QFY07-03, 2022QFY07-06) and the Shaanxi Province Training Program of Innovation and Entrepreneurship for Undergraduates (S202210719108), the Foundation of State Key Laboratory of Coal Conversion (grant number J24-25-909), the Natural Science Research Foundation of Shanxi Province (202303021211016).

Author contributions

F.F., H.Y., and C.Y. conceived and supervised the project. Y.L. and F.Y. executed the experiments and collected the data. T.L. and Y.J. conducted the theoretical calculations. Y.-C.H. carried out the EXAFS characterization measurements. All authors edited the paper.

Competing interests

The authors declare no conflict of interest.

Additional information

Supplementary information The online version contains supplementary material available at https://doi.org/10.1038/s41467-025-57097-x.

Correspondence and requests for materials should be addressed to Feng Fu, Yu Jing, Hengquan Yang or Chunming Yang.

Peer review information *Nature Communications* thanks the anonymous reviewers for their contribution to the peer review of this work. A peer review file is available.